Radiofrequency sheath rectification on WEST: application of the sheath-equivalent dielectric layer technique in tokamak geometry

W. Tierens, A. Kumar, C. Klepper, J. Lore, J.R. Myra, J. Hillairet, Guillaume Urbanczyk, W. Helou, L. Colas, A. Grosjean, et al.

PAPER • OPEN ACCESS

Radiofrequency sheath rectification on WEST: application of the sheath-equivalent dielectric layer technique in tokamak geometry*

To cite this article: W. Tierens *et al* 2024 *Nucl. Fusion* **64** 126039

OPEN ACCESS
IOP Publishing | International Atomic Energy Agency
Nuclear Fusion
Nucl. Fusion **64** (2024) 126039 (13pp)
https://doi.org/10.1088/1741-4326/ad80a9

Radiofrequency sheath rectification on WEST: application of the sheath-equivalent dielectric layer technique in tokamak geometry*

W. Tierens[1,], A. Kumar[1], C. Klepper[1], J. Lore[1], J.R. Myra[2], J. Hillairet[3], G. Urbanczyk[4], W. Helou[5], L. Colas[3], A. Grosjean[6], J. Gunn[3] and the WEST Team[a]**

[1] Oak Ridge National Laboratory, 1 Bethel Valley Road, Oak Ridge, TN 37830, United States of America
[2] Lodestar Research Corporation, 5055 Chaparral Ct, Ste 102, Boulder, CO 80301, United States of America
[3] CEA, IRFM, F-13108 St-Paul-Lez-Durance, France
[4] IJL, UMR 7198, CNRS-U, de Lorraine, F-54506 Vandoeuvre Cedex, France
[5] ITER Organization, Route de Vinon-sur-Verdon, CS 90 046, 13067 St. Paul Lez Durance Cedex, France
[6] Department of Nuclear Engineering, The University of Tennessee Knoxville, Knoxville, TN 37996, United States of America

E-mail: tierenswv@ornl.gov

Received 23 April 2024, revised 4 September 2024
Accepted for publication 27 September 2024
Published 14 October 2024

Abstract

Radiofrequency sheath rectification is a phenomenon relevant to the operation of Ion Cyclotron Range of Frequencies (ICRFs) actuators in tokamaks. Techniques to model the sheath rectification on 3D ICRF antenna geometries have only recently become available (Shiraiw *et al* 2023 *Nucl. Fusion* **63** 026024; Beers *et al* 2021 *Phys. Plasmas* **28** 093503). In this work, we apply the 'sheath-equivalent dielectric layer' technique, used previously only on linear devices (Beers *et al* 2021 *Phys. Plasmas* **28** 103508), in tokamak geometry, computing rectified sheath potentials on the WEST ICRF antenna. Advancing the state of the art in sheath rectification modeling, we compute the sheath potentials not just on the limiters, but also on the Faraday Screen bars. The calculations show a peak rectified DC potential of 300 V on the limiters and 500 V on the Faraday screen. Assuming a typical sputtering yield curve, the RF sheath

[a] See http://west.cea.fr/WESTteam.

* This manuscript has been authored in part by UT-Battelle, LLC, under Contract DE-AC05-00OR22725 with the US Department of Energy (DOE). This material is based upon work supported by the U.S. Department of Energy, Office of Science, Office of Advanced Scientific Computing Research and Office of Fusion Energy Sciences, Scientific Discovery through Advanced Computing (SciDAC) program. The publisher acknowledges the US government license to provide public access under the DOE Public Access Plan (http://energy.gov/downloads/doe-public-access-plan). The views and opinions expressed herein do not necessarily reflect those of the ITER Organization.

** Author to whom any correspondence should be addressed.

rectification increases the sputtering yield from the limiters by a factor of 2.6 w.r.t. the sputtering due to the non-rectified thermal sheath.

Keywords: ICRF, sheaths, PMI

(Some figures may appear in colour only in the online journal)

1. Introduction

The numerical modeling of the emission of radiofrequency (RF) electromagnetic waves from an Ion Cyclotron Range of Frequencies (ICRFs) actuator in a tokamak or stellarator is an important task for which various simplifying assumptions may be well-justified, depending on the physical quantities of interest. If we are chiefly interested in the power coupled to the plasma, it is entirely justified to put Perfect Electric Conductor (PEC) boundary conditions on the antenna surface, and even to keep the antenna in vacuum, while still getting physically correct predictions, even in highly nontrivial plasma conditions, such as those involving gas puffing or resonant magnetic perturbations [1–4]. This is because ICRF power coupling is mainly determined by the fast wave evanescence in front of the antenna [5], with some minor dependence on the gradient [6], but neither the edge physics nor the core absorption plays much of a role.

If we are interested in finer details of the edge physics, such as sheath formation and rectification on the antenna surfaces, and the associated possibility of increased impurity sputtering, we need to impose a sheath boundary condition [7] on the antenna surface. This boundary condition gives the tangential electric field E_t as a function of the sheath impedance z_sh and the normal RF current J_n,

$$E_\mathrm{t} = \nabla\left(z_\mathrm{sh} J_\mathrm{n}\right). \tag{1}$$

Actually implementing this boundary condition in numerical frequency-domain RF solvers proved to be difficult, especially in 3D (the first 3D time-domain implementations [8] precede the first 3D frequency-domain implementations by 5 years). For most of the 2010 s, most researchers resorted to 2D approaches. This includes the 'SSWICH' code [9–11] for modeling of experiments and antenna designs, the 'rfSOL' code [12, 13] for fundamental research, and more recently the 'Stix' code [14].

The first proof-of-concept implementation of a 3D frequency-domain solver which could handle (1), albeit only in severely restricted geometries, was [15]. Later, [16] managed to implement this boundary condition, for general geometries, in the Petra-M code. Both approaches give consistent results in good agreement with experimental data on ASDEX Upgrade [17].

Another effort to avoid the difficulty of a direct implementation of (1) is based on placing a dielectric layer with finite thickness (much thicker than the physical sheath thickness $\approx$ the Debye length, yet much thinner than the other length scales in the antenna geometry), which plays the role of the sheath, in the simulation domain. By giving this dielectric layer appropriate 'sheath-mimicking' material properties (ϵ, σ), the sheath boundary condition can be self-consistently approximated, without implementing it as a boundary condition per se. This approach [19] was applied successfully on the linear device Proto-MPEX [20] and more recently on PISCES-RF [18, 21]. In this work, we apply it for the first time in a tokamak geometry.

Sheath rectification calculations are typically performed on the ICRF antenna limiters. This is both due to inherent limitations in the traditional approaches to sheath modeling, which were specialized for that particular task and could not handle the greater geometric complexity of the rest of the antenna, but it is also physically justified: the limiters are where most sheath rectification is to be expected, and where sheath rectification should most contribute to impurity sputtering. In addition, the validity of the sheath boundary condition is assured on the limiter sides [22], but not on other surfaces which may be near parallel to the magnetic field ('magnetic tangency points', see figure 1).

In this work, we will compute the rectified DC potential on both the limiters and on the Faraday Screen bars, mainly to demonstrate the geometric flexibility of our approach. While erosion from the Faraday Screen bars should usually be quite limited, there are other physical reasons to be interested in V_DC there:

- Computing the sheaths and associated impurity release on the Faraday Screen could provide insight on previous experimental results, comparing impurity release with and without the Faraday Screen.
- Sheaths on the Faraday Screen bars might generate convective cells which could transport plasma into that region.
- If the Faraday Screen is not perfectly parallel to the confining magnetic field, there may be field lines that connect a Faraday Screen bar to a side limiter or septum. Such sheaths could have high voltages.

2. Finite element model of the WEST antenna

We imported a CAD model of the WEST ICRF antenna [23, 24] (the same one used in [16]) into the COMSOL finite element software, and built a toroidal approximation of the vessel around it, as shown in figure 2. This toroidal approximation of the more complicated true vessel shape is intended to allow for the construction of toroidal Perfectly Matched Layers (PMLs) [25], which allow us to terminate the simulation domain without including the geometry of the full torus and without having to model core absorption, an approach used previously on ASDEX Upgrade [2].

The nested flux surfaces along which the plasma parameters are assumed constant are also approximated as nested circular

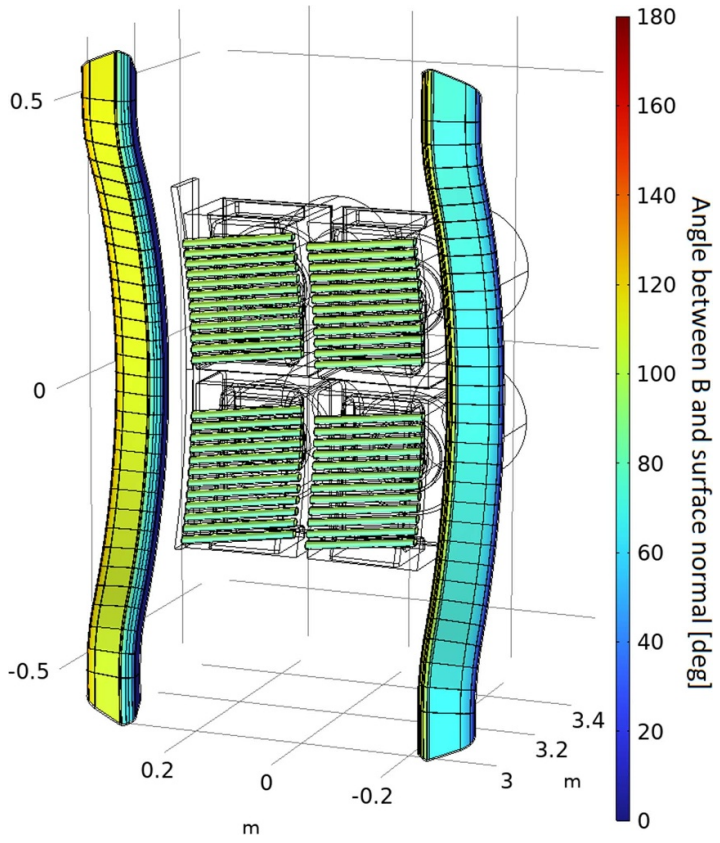

Figure 1. The angle between the magnetic field and the surface normal. 90° is magnetic tangency, at which the applicability of the local sheath boundary condition is in doubt.

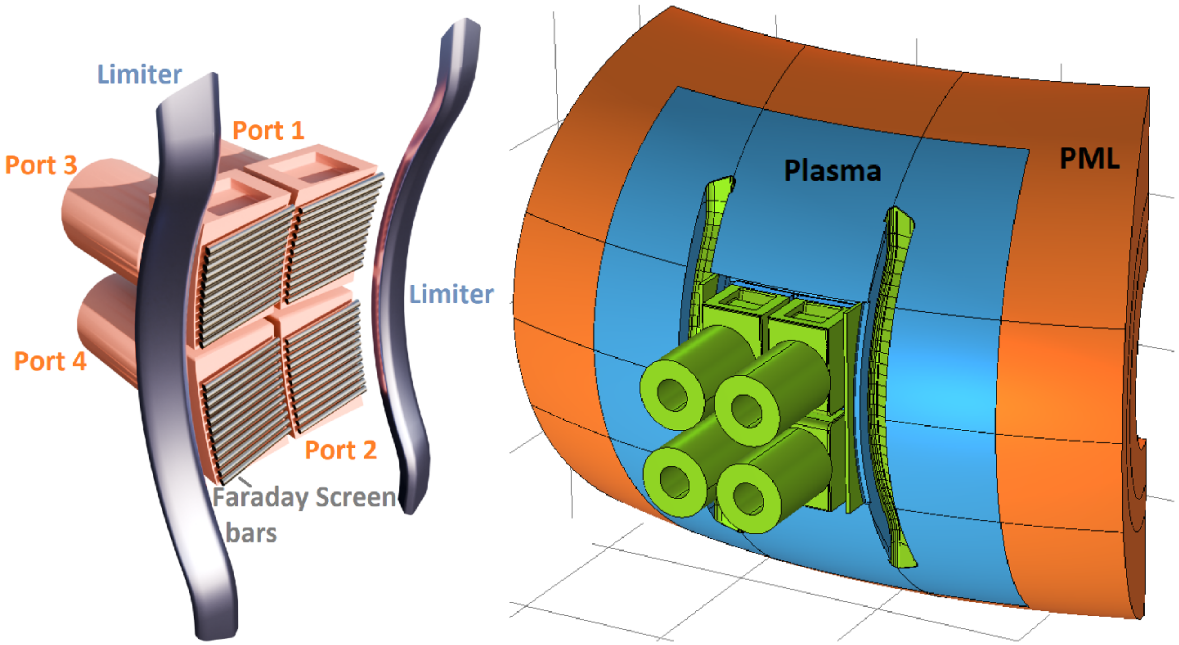

Figure 2. Left: CAD model of the WEST ICRF antenna geometry. The ports, limiters, and Faraday Screen bars are labeled. Right: the WEST ICRF antenna model inside its toroidal vessel.

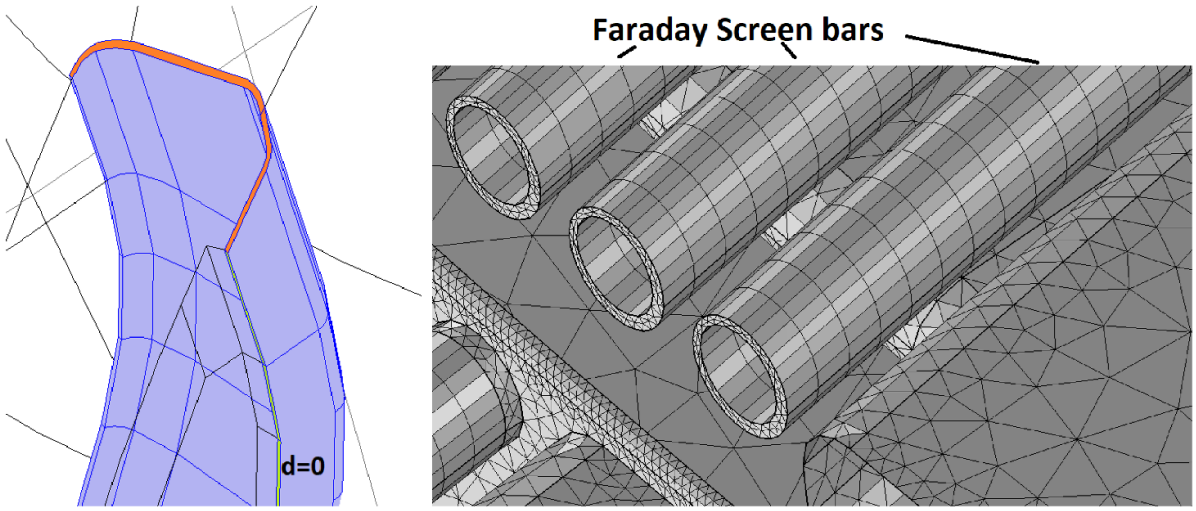

Figure 3. Left: we construct an artificial 'sheath layer' on the limiters. It is 2 mm thick. Within it, we will define an isotropic dielectric material to mimic the much thinner physical sheath. Right: we also construct an artificial sheath layer on the Faraday Screen bars. Note that the artificial sheath thickness need not be constant. In this geometry, it is constant along the limiters, but not along the Faraday Screen bars..

tori, using three measurements of the major radius coordinate of a surface of constant density, at three vertical locations, from WEST shot 57877. This means that deviations from axisymmetry are not taken into account in the plasma model.

In WEST, the antennas can be moved radially. We adjusted the geometry to account for the radial position of the antenna, as it was in shot 57877: the major radius coordinate of the tip of the lateral limiter in the equatorial plane was 3.011 m.

In order to apply the sheath-equivalent dielectric layer technique, we have extruded the limiter surfaces to a finite thickness of 2 mm as shown in figure 3, such that we can include a sheath-mimicking material in that layer. Similarly, we meshed a thin layer around each Faraday Screen bar, which will enable us to compute the rectified sheath potentials there as well.

3. Coordinatizing the limiter surfaces: the Eikonal equation

The sheath model [26] computes the rectified sheath voltage and RF sheath impedance parameter z_{sh} to be used in equation (1). The sheath impedance may be converted to equivalent material layer parameters, the permittivity ε and the conductivity σ, in a manner that allows the dielectric layer to mimic the RF impedance properties of the sheath. See [19] for details. Our implementation is based upon that of [19], with major modifications to handle the complex tokamak geometry. These quantities are not constant; ϵ and σ vary along the sheath surfaces. For this reason it is necessary to coordinatize these surfaces: we must have a 2D coordinate system on the sheath surfaces such that we may interpolate ϵ and σ to any point on those surfaces. In linear devices such as Proto-MPEX and PISCES-RF, where this approach was applied before [20], the sheath surface is a cylinder, and this coordinatization is trivial.

In the more complicated case of WEST, we decided to construct this coordinate system numerically. We choose one coordinate to be the poloidal angle, and the other one, a 'toroidal distance along the limiter', we determine by numerically solving the Eikonal equation in the sheath layer

$$|\nabla d| = 1 \tag{2}$$

with $d = 0$ along the antenna-facing boundary of the sheath layer (green in figure 3) and $(\nabla d) \cdot n = 0$ on the other boundaries. The Eikonal equation (2) defines the signed distance from the $d = 0$ boundary (the distance along the limiter surface, not the 3D Euclidean distance), hence the d field solution of (2) is interpretable as a coordinate. Figure 4 shows these coordinates. We also define cylindrical coordinates for each Faraday Screen bar.

4. Physical parameters

We make use of a 1D density profile obtained from reflectometry in WEST shot 57877, shown in figure 5 and mapped to the 3D antenna structures in figure 6. Using this density we construct the usual cold plasma dielectric tensor [27]

$$\epsilon = \begin{bmatrix} S & -iD & 0 \\ iD & S & 0 \\ 0 & 0 & P \end{bmatrix} \tag{3}$$

to characterize the electromagnetic behavior of the plasma.

The notoriously problematic [28] $S = 0$ layer occurs between the Faraday Screen and the straps. In conventional ICRF operation, it is more common that $S = 0$ occurs between the Faraday Screen and the core plasma. In order to avoid numerical challenges associated with the Lower Hybrid resonance at $S = 0$, we make use, as is conventional, of a discontinuous jump between plasma and vacuum (a plasma-vacuum interface [1, 29]), but, because of the unusual location of

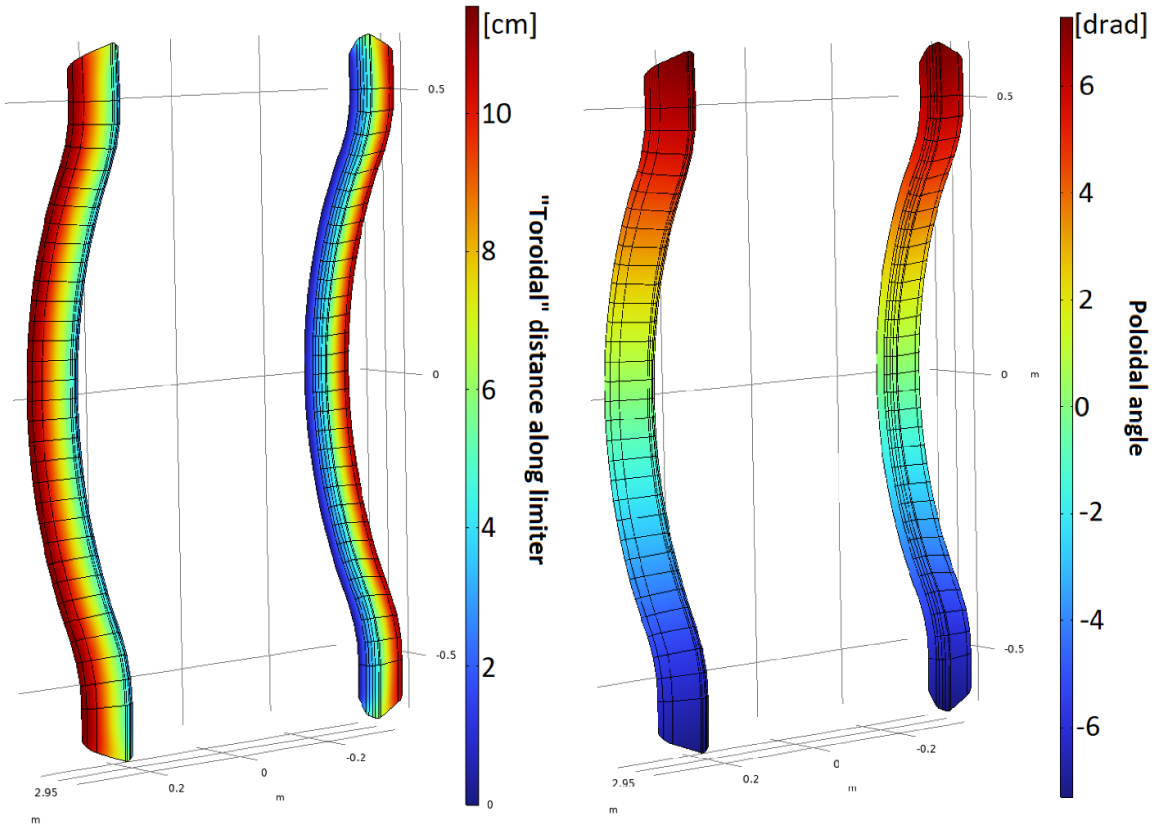

Figure 4. Numerical coordinatization of the limiter surfaces. The 'toroidal' distance along the limiter (left) is determined by solving the Eikonal equation (2) numerically. For the second coordinate on the limiter surface, we use the poloidal angle (right).

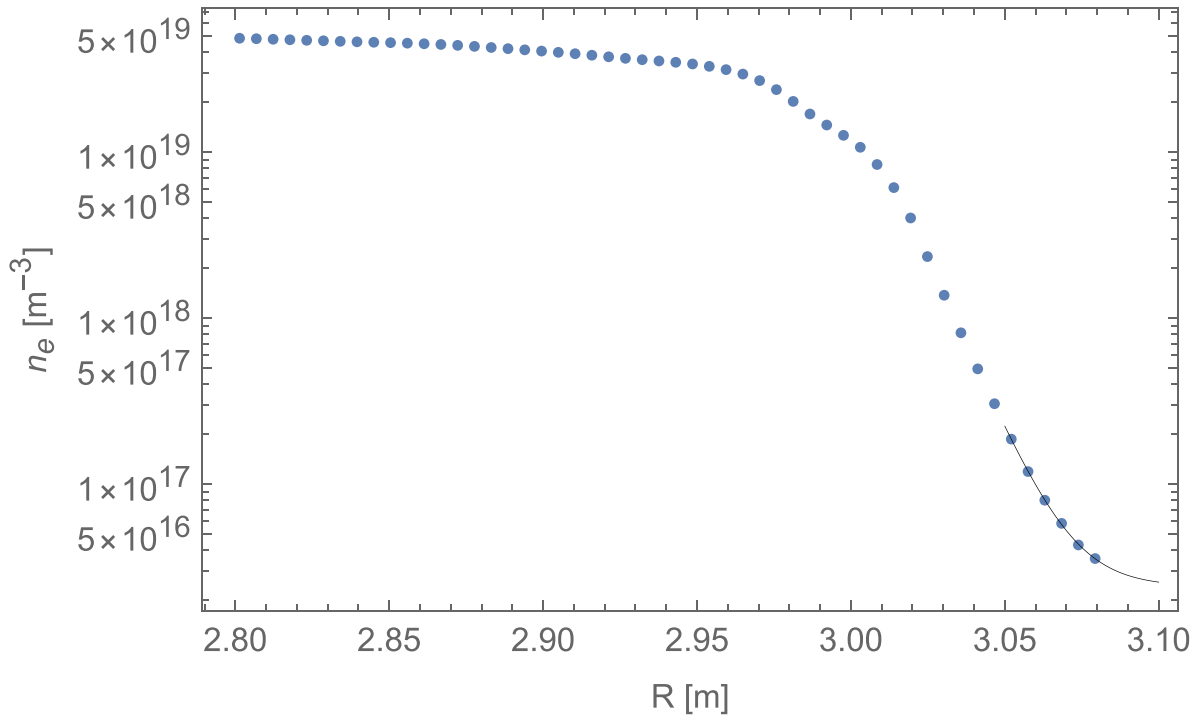

Figure 5. Electron density vs. major radius coordinate, obtained from reflectometry on WEST shot 57877, smoothly extrapolated as $10^{19}\exp(-97.6017(R-3.00988))+2.41528\cdot10^{16}$ in the low-density limit.

$S = 0$, we can place the plasma-vacuum interface between the Faraday Screen and the straps. This is shown in figure 7.

This point deserves some discussion. The conventional approach to ICRF antenna modeling, at least where the prediction of the coupled power is concerned, relies on having a plasma-vacuum interface between the plasma and the antenna. This is true both for finite element approaches [1], and in other approaches [30]. This approach gives surprisingly good agreement with experiment, even in complex 3D plasma scenarios [2, 4], lending credibility to the claim that the only thing that matters for coupling is the thickness of the evanescence layer [5], and that the edge physics does not matter (for the coupling). For our purposes here, the sheaths, the edge physics clearly does matter and we can no longer keep the antenna entirely in vacuum. Figure 7 represents the best-case scenario: we can still do a plasma-vacuum jump which skips the Lower Hybrid resonance [28] and related resonances [31], this interface does not intersect crucial antenna components (Faraday Screen bars, straps), and we do not need to introduce large edge losses (which would contradict the observation that we get the correct coupling with zero edge losses if we use the conventional vacuum layer approach).

Assuming that this density profile remains valid even inside the antenna (as opposed to assuming a steeper decay inside the antenna), we can now take the physically correct approach: we solve Maxwell's equations in a relatively dense plasma near the antenna, and couple it to the sheath model which gets the same density as input. The opposite approach, i.e. solving Maxwell's equations in vacuum and using the resulting vacuum fields to excite a non-vacuum sheath model, has historically been common. For example, all SSWICH calculations take vacuum fields computed in either RAPLICASOL or TOPICA as input.

The electron temperature profile is not available for this shot. This is because the pecker probes [32], which usually measure this quantity on WEST, cannot compensate for the rectified sheath potentials during ICRF operation. We have thus assumed a constant electron temperature $T_e = 10\,\mathrm{eV}$.

In shot 57877, the measured total voltages V_{tot} in each of the four ports were 26 kV, 24 kV, 28 kV, and 26.5 kV respectively. From our model we obtained the 4×4 S-matrix

$$\begin{bmatrix} 0.25 + 0.92i & (1.1 + 0.44i)\,10^{-2} & (4.14 + 0.84i)\,10^{-3} & (1.61 + 1.48i)\,10^{-3} \\ (3.13 - 8.71i)\,10^{-4} & 0.26 + 0.92i & (8.38 - 15.1i)\,10^{-5} & (5.67 + 1.11i)\,10^{-3} \\ (35.3 - 3.37i)\,10^{-4} & (2.72 + 1.62i)\,10^{-3} & 0.26 + 0.92i & (1.09 + 0.44i)\,10^{-2} \\ (6.83 - 16.3i)\,10^{-5} & (5.25 + 0.05i)\,10^{-3} & (3.22 - 8.79i)\,10^{-4} & 0.26 + 0.92i \end{bmatrix} \tag{4}$$

and derive incident amplitudes V_i such that $V_{tot} = |V_i + SV_i|$. Together with dipole phasing, this gives $V_i = 16.8\,\mathrm{kV}$, $-15.4\,\mathrm{kV}$, $-18.1\,\mathrm{kV}$, and $17\,\mathrm{kV}$ for ports 1 through 4 respectively (see figure 2 for the port indices).

5. Iterating the sheath model

At each iteration, the sheath model [19, 26] gives us the dielectric parameters ϵ and σ to be imposed in the sheath layers. Re-running the simulation with these new material parameters then gives us an updated RF sheath voltage (i.e. the normal RF electric field in the sheath layers times the layer thickness), from which we re-calculate ϵ and σ until convergence is reached, as in figure 8. Figure 9 shows the normal RF electric field and the rectified DC potential at the fourth iteration.

We see that V_{DC} on the limiters converges to a peak value of about 300 V, while V_{DC} on the Faraday Screen peaks at a substantially higher value of about 500 V, though the latter needs to be taken with a grain of salt because the Faraday Screen bars are nearly parallel to the confining magnetic field, and also because we assumed a constant T_e even though T_e at the Faraday Screen bars is, in reality, probably lower than at the limiters.

We intend to use this V_{DC} as input to a sophisticated sputtering code in future work. For now, as a first step, we take a WEST-relevant sputtering yield curve [33] $Y_{eff}(V_{DC})$ shown in figure 10, which gives the number of atoms sputtered per incident ion, given the incident ion energy eV_{DC} (for a singly charged ion). $Y_{eff}(V_{DC}) n_i \sqrt{3T_i/m_i}$ is then a measure for the number of atoms sputtered per surface area per second. The integral of this quantity over the sheath surfaces, i.e. the total number of atoms sputtered per second, is $1.6 \cdot 10^{17}\,\mathrm{s}^{-1}$ for the limiters, and $4.9 \cdot 10^{17}\,\mathrm{s}^{-1}$ for the Faraday Screen bars (with the usual caveats that the sheath model may not be fully applicable there due to the magnetic field being near parallel to the surface, and our assumption of a constant $T_i = T_e = 10\mathrm{eV}$, in reality the plasma at the Faraday Screen is probably colder than at the limiters). In the presence of only the non-rectified thermal sheath, the same calculation yields $6.2 \cdot 10^{16}\,\mathrm{s}^{-1}$ atoms sputtered per second from the limiters, and $3.7 \cdot 10^{16}\,\mathrm{s}^{-1}$ from the Faraday Screen. So, the RF rectification increases the total sputtering from the limiters by a factor 2.6, and from the Faraday Screen by a factor 13.2.

6. Conclusion

We have applied, for the first time, the sheath-equivalent dielectric layer technique in a tokamak geometry. This technique allows greater geometric complexity than most previous approaches. We have made use of this to compute rectified

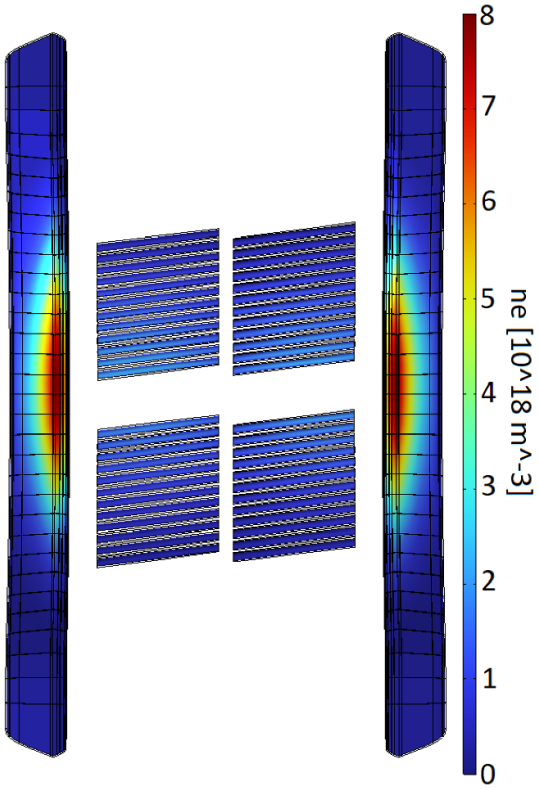

Figure 6. Density $[10^{18}\mathrm{m}^{-3}]$ shown along the limiter and Faraday Screen surfaces. The 3D density is reconstructed by using the density profile from figure 5 and assuming constant density along the flux surfaces. The density along these surfaces corresponds to 3.01 m $< R <$ 3.18 m in figure 5.

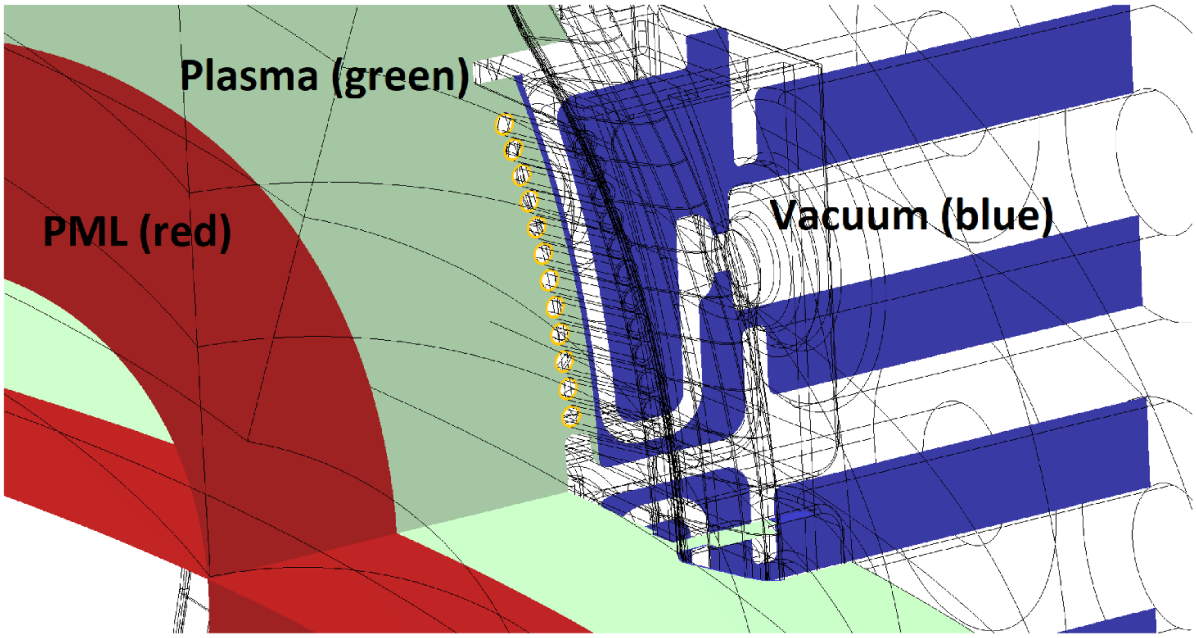

Figure 7. The plasma-vacuum interface, the discontinuous transition from plasma (green) to vacuum (blue) occurs in an unusual location in our model: it is between the Faraday Screen and the antenna straps. The yellow rings surrounding the Faraday Screen bars denote the thin layer of sheath-mimicking material.

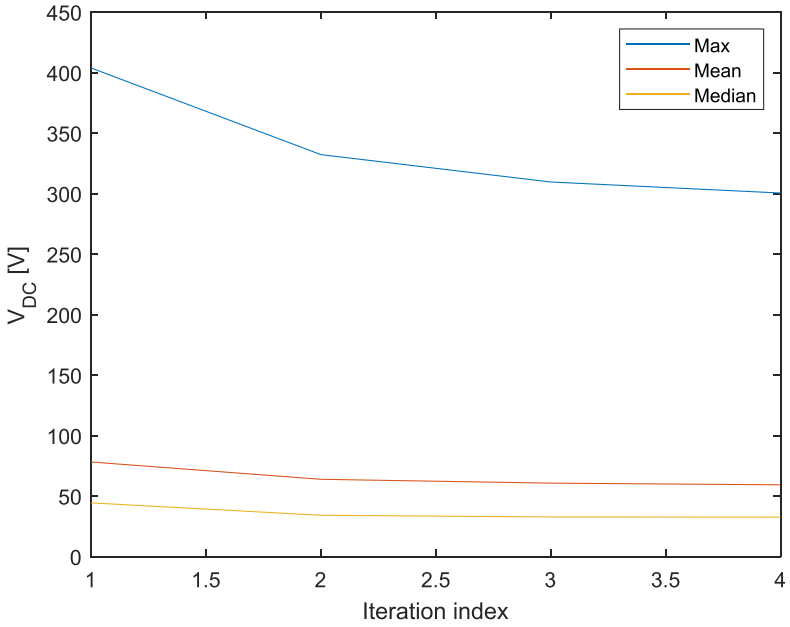

Figure 8. Maximum, mean, and median V_{DC} as we iterate the sheath model. The difference between iteration 3 and iteration 4 is below 3%. The main results shown in this work are at iteration 4.

sheath potentials on both the limiters and the Faraday Screen bars of an ICRF antenna.

In future work, we intend to compare the results with experimental data, and/or use the rectified sheath potential as input to the GITR sputtering code [34], with the ultimate goal of enabling predictive quantitative modeling of RF-induced impurity sputtering.

Acknowledgments

This manuscript has been authored by UT-Battelle, LLC, under Contract No. DE-AC05-00OR22725 with the U.S. Department of Energy (DOE). This material is based upon work supported by the U.S. Department of Energy, Office of Science, Office of Advanced Scientific Computing Research and Office of Fusion Energy Sciences, Scientific Discovery through Advanced Computing (SciDAC) program.

The views and opinions expressed herein do not necessarily reflect those of the ITER Organization.

Appendix A. Vertical symmetry

Neither the antenna geometry nor the density are exactly vertically symmetric. Still, the density (figure 6) is closer to vertically symmetric than usual for WEST, the center of the nested flux surfaces along which the density is constant being only 0.6 cm away from the $y = 0$ plane (y being the vertical axis in this geometry). Yet, the electric field and V_{DC} in figure 9 are highly asymmetric, peaking at the top rather than the bottom of the antenna. To investigate this, we have moved the density vertically by ± 5 cm as shown in figure A1. The effect of this change in density on the RF electric field at the sheath surfaces (at the first iteration, when the sheath layers are still vacuum) is shown in figure A2.

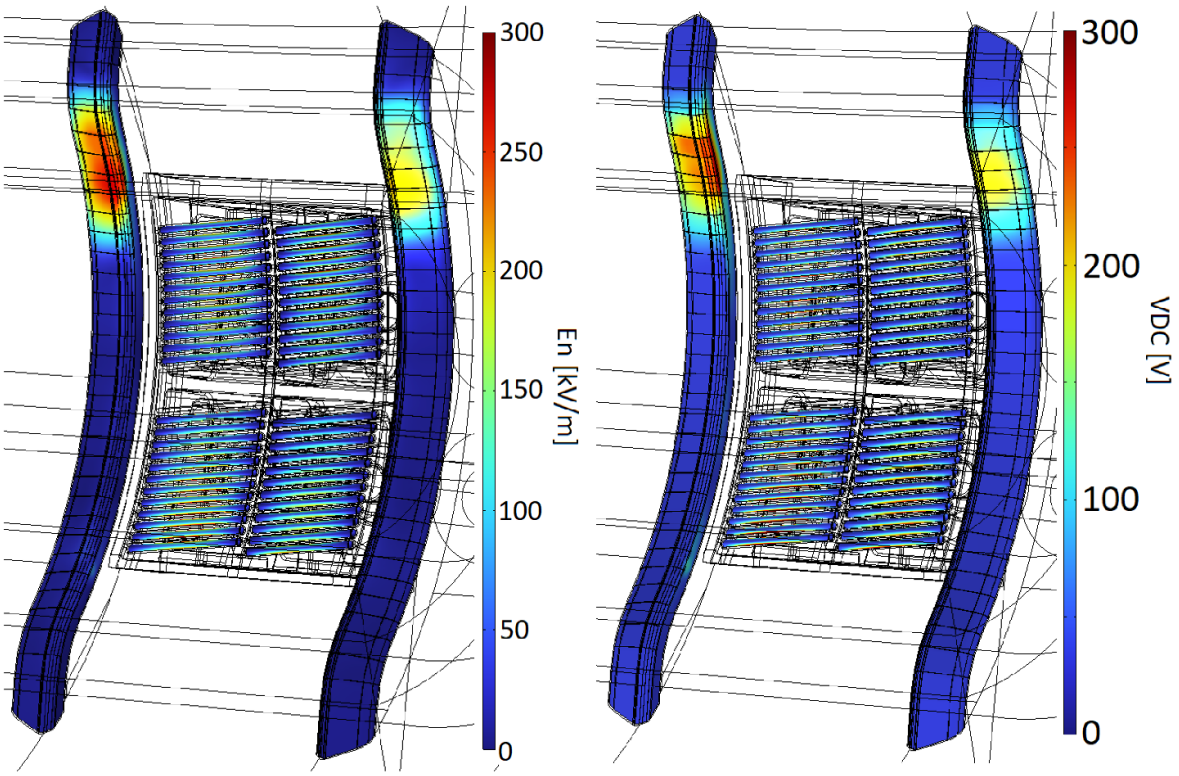

Figure 9. Left: normal RF electric field (kV m^{-1}) along the sheath surfaces. Right: rectified sheath potential V_{DC} [V] on the limiters and Faraday Screen bars of our model of the WEST antenna.

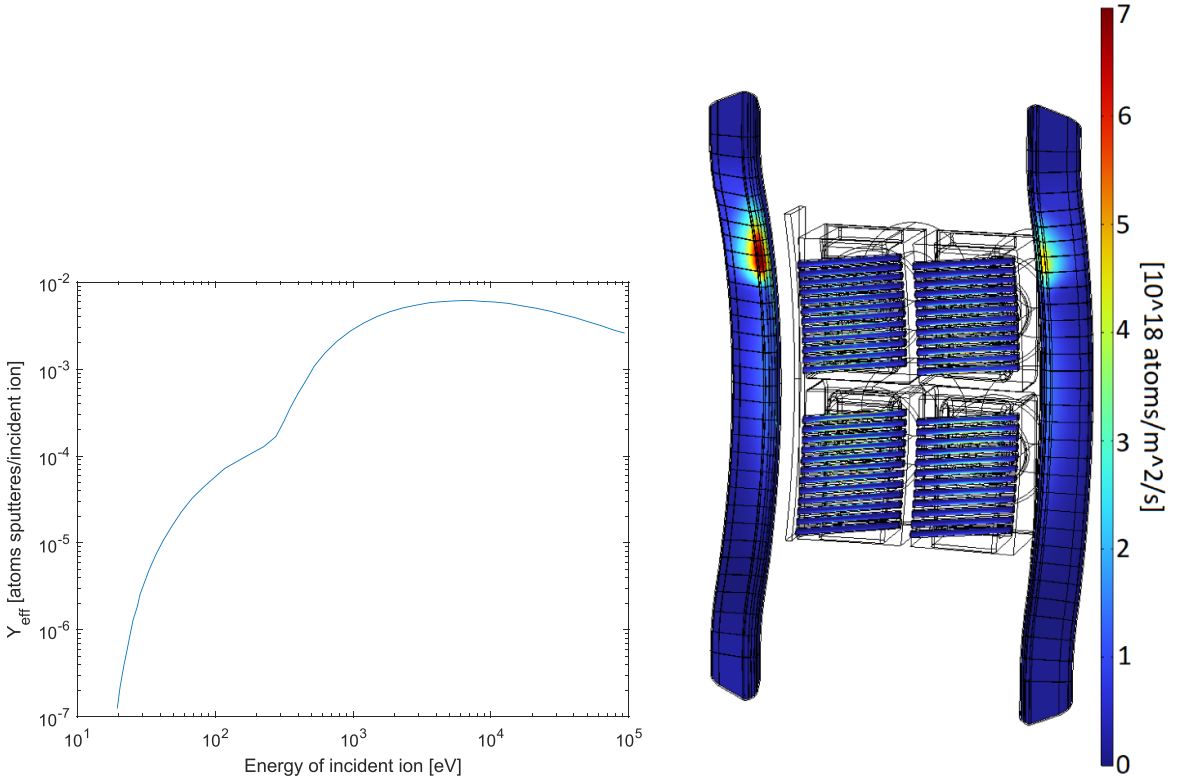

Figure 10. Left: $Y_{\mathrm{eff}}(V_{\mathrm{DC}})$, an effective sputtering curve typical for WEST, assuming a Deuterium plasma with 4% H, 0.05% B, 0.05% C, and 0.001% W. Right: $Y_{\mathrm{eff}}(V_{\mathrm{DC}})n_i\sqrt{3T_i/m_i}$, a measure for the number of atoms sputtered per m^2 per second.

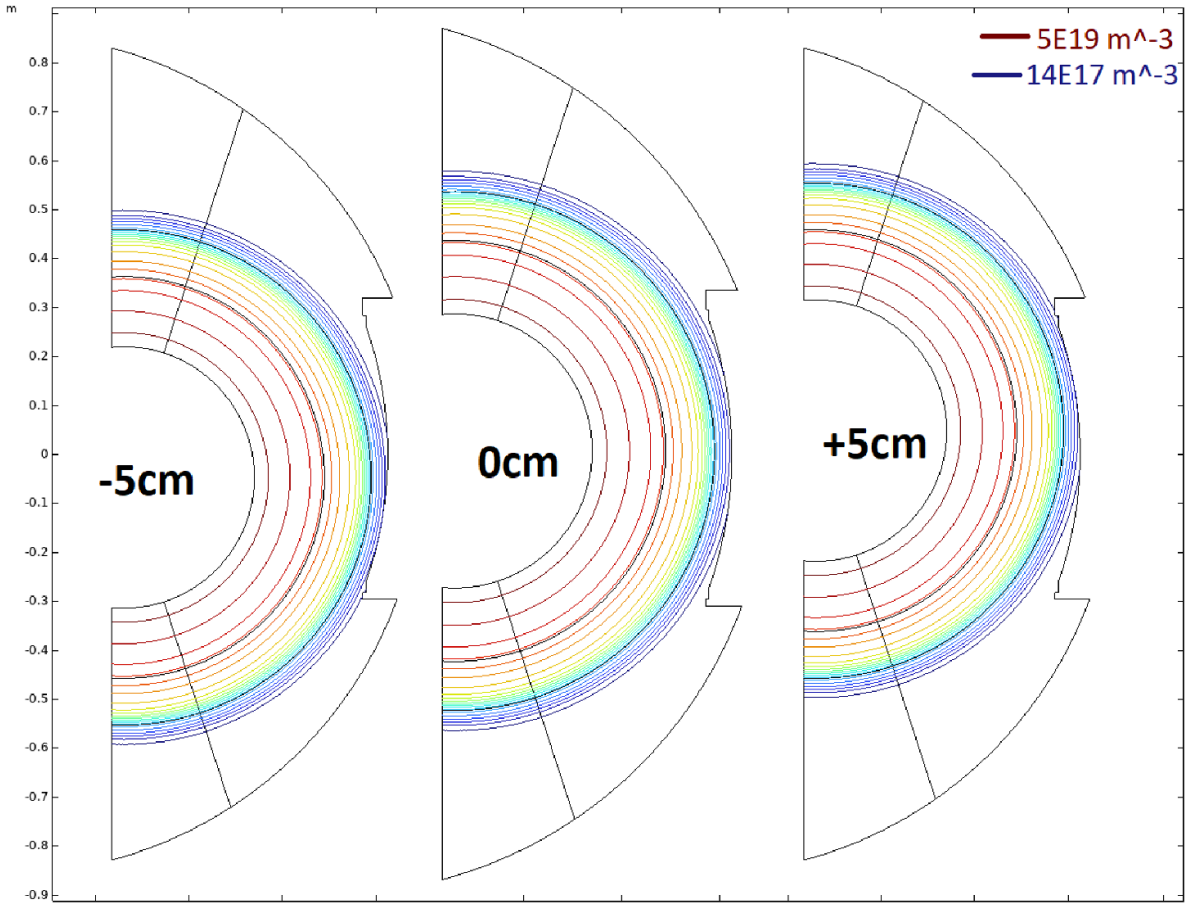

Figure A1. Contours of constant density, left: shifted downward by 5 cm, middle: not shifted (matches experiment, this is the one used throughout this work), right: shifted upward by 5 cm.

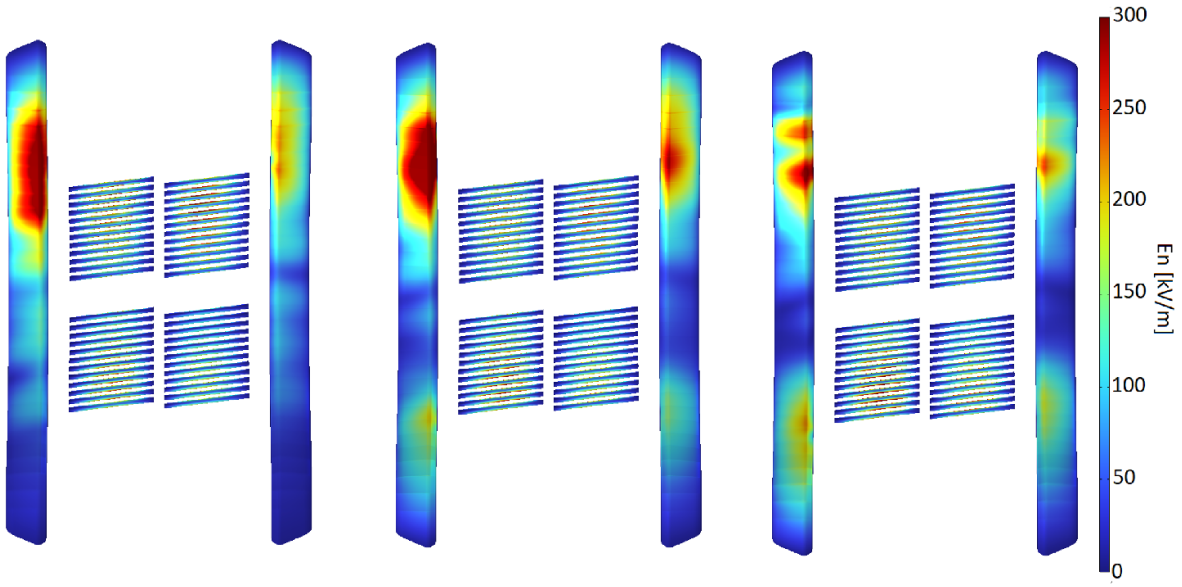

Figure A2. Radiofrequency electric field strength $|E|$ (kV m^{-1}) on the sheath surfaces for the three density cases of figure A1.

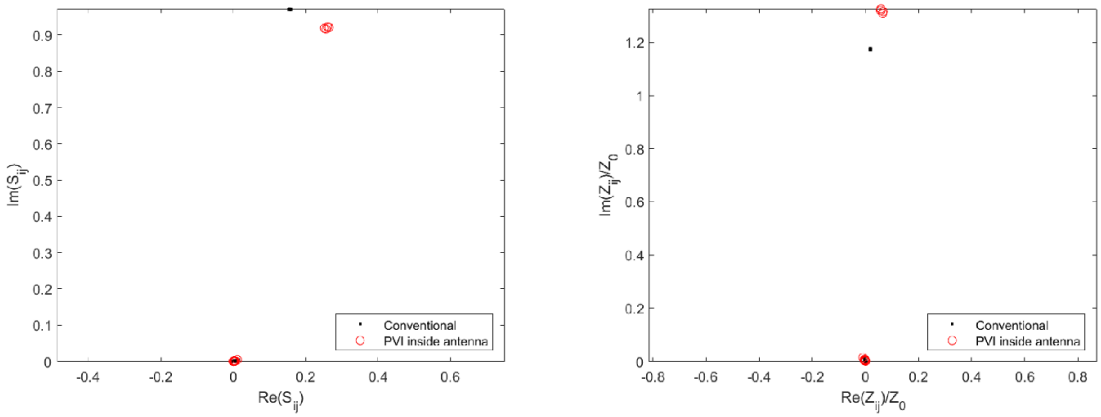

Figure B.1. Comparison of the 4×4 complex S- and Z-matrix entries, computed with the plasma-vacuum interface inside the antenna as in this work (see figure 7), vs. outside the antenna, as is conventional.

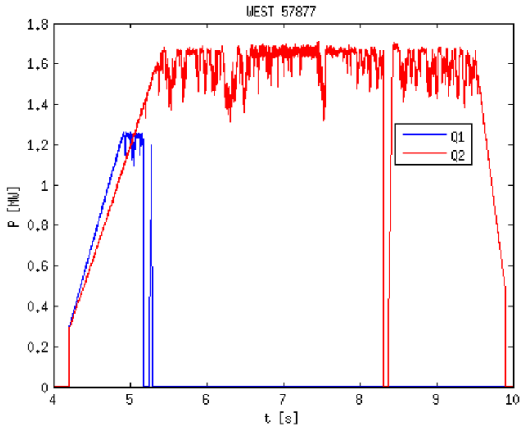

Figure B.2. Power coupled by two active ICRF antennas during WEST shot 57877.

Appendix B. Influence of the location of the plasma-vacuum interface on the coupled power

We derived our S-matrix (4) from a model in which the plasma-vacuum interface is in an unconventional location (figure 7). To the extent that such S-matrix calculations have been successfully compared with experiment, this has been done with models where the plasma-vacuum interface is in the conventional location, in front of the antenna, such that the entire antenna is in vacuum. To check if our S-matrix calculation makes sense, we compare with a conventional calculation where the plasma-vacuum interface is in its conventional location, outside the antenna. This comparison is shown in figure B.1. For the same incident amplitudes as before, $V_i =$ 16.8 kV, -15.4 kV, -18.1 kV, and 17 kV for ports 1 through 4, the coupled power is 1 MW for the plasma-vacuum interface inside the antenna, and 0.5 MW for the conventional plasma-vacuum interface. The former is closer to the experimentally measured coupled power, which was over 1 MW in this experiment, see figure B.2.

Appendix C. Insensitivity to artificial sheath thickness parameter *d*

The results should be approximately independent of the thickness of the sheath-mimicking layers, provided they are thin enough. As the sheath layers on the FS bars were constructed manually, we cannot easily modify it. The sheath layer on the limiters, on the other hand, was constructed procedurally, so we can adjust it with ease. In the rest of this work, we used $d = 2$ mm for the sheath layer thickness on the limiters. In this appendix, we modify it to $d = 1$ mm to verify insensitivity of the result to d. The result in figure C.1 indeed confirms that the results are insensitive to d.

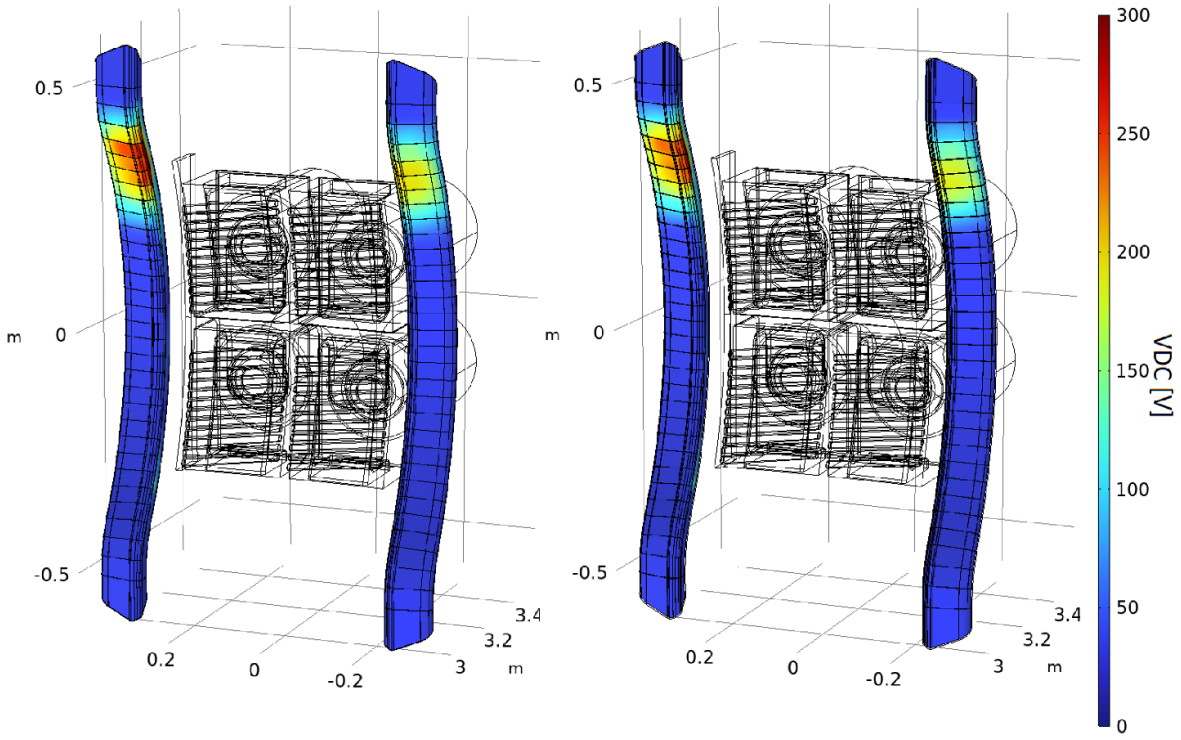

Figure C.1. Left: V_{DC} after four iterations with $d = 1$ mm. Right: V_{DC} after four iterations with $d = 2$ mm (same parameters as in figure 9).

ORCID iDs

W. Tierens https://orcid.org/0000-0002-6979-8140
C. Klepper https://orcid.org/0000-0001-9107-8337
J. Lore https://orcid.org/0000-0002-9192-465X
J.R. Myra https://orcid.org/0000-0001-5939-8429
J. Hillairet https://orcid.org/0000-0002-1073-6383
G. Urbanczyk https://orcid.org/0000-0002-4026-6802
L. Colas https://orcid.org/0000-0002-4573-3326

References

[1] Tierens W. *et al* 2019 *Nucl. Fusion* **59** 046001
[2] López G.S. *et al* 2020 *Plasma Phys. Control. Fusion* **62** 125021
[3] Tierens W., Jacquot J., Zhang W., Noterdaeme J.M., Bobkov V. and Colas L. 2017 3-dimensional density profiles in edge plasma simulations for ICRF heating *EPJ Web of Conferences* vol 157 (EDP Sciences) p 03053
[4] Zhang W. *et al* 2017 *Plasma Phys. Control. Fusion* **59** 075004
[5] Bilato R., Brambilla M., Hartmann D. and Parisot A. 2005 *Nucl. Fusion* **45** L5
[6] Messiaen A. and Weynants R. 2011 *Plasma Phys. Control. Fusion* **53** 085020
[7] Myra J. 2021 *J. Plasma Phys.* **87** 905870504
[8] Smithe D.N., D'Ippolito D.A. and Myra J.R. 2014 Quantitative modeling of ICRF antennas with integrated time domain RF sheath and plasma physics *AIP Conf. Proc.* **1580** 89–96
[9] Lu L. *et al* 2018 *Plasma Phys. Control. Fusion* **60** 035003
[10] Křivská A., Bobkov V., Colas L., Dumortier P., Durodié F., Lerche E., Jacquet P., Jacquot J., Klepper C. and Milanesio D. 2017 Electromagnetic simulations of JET ICRF ITER-like antenna with TOPICA and SSWICH asymptotic codes *EPJ Web of Conferences* vol 157 (EDP Sciences) p 03026
[11] Tierens W. *et al* 2017 *Nucl. Fusion* **57** 116034
[12] Kohno H., Myra J. and D'Ippolito D. 2012 *Phys. Plasmas* **19** 012508
[13] Kohno H. and Myra J. 2019 *Phys. Plasmas* **26** 022507
[14] Migliore C., Wright J., Stowell M. and Bonoli P. 2023 *Nucl. Fusion* **63** 106006
[15] Tierens W., Urbanczyk G., Colas L. and Usoltceva M. 2019 *Phys. Plasmas* **26** 083501
[16] Shiraiwa S., Bertelli N., Tierens W., Bilato R., Hillairet J., Myra J., Kohno H., Poulos M. and Ono M. 2023 *Nucl. Fusion* **63** 026024
[17] Urbanczyk G., Ochoukov R., Bobkov V., Shiraiwa S., Bilato R., Bertelli N., Tierens W., Colas L. and Helou W. 2024 in preparation
[18] Dhamale G., Baldwin M., ISLAM M.S., Kumar A., Patino M., Tierens W. and Rapp J. 2023 *J. Am. Phys. Soc.* **2023** pp 11–125
[19] Beers C.J., Green D.L., Lau C., Myra J., Rapp J., Younkin T.R. and Zinkle S.J. 2021 *Phys. Plasmas* **28** 093503
[20] Beers C. *et al* 2021 *Phys. Plasmas* **28** 103508
[21] Dhamale G., Baldwin M., Islam M.S., Kumar A., Meyer H.M., Nishijima D., Patino M., Tierens W. and Rapp J. 2023 *Understanding Impurity Transport in PISCES-RF Device 8th Int. Workshop on Plasma Material Interaction Facilities for Fusion Research*
[22] Myra J.R. and Kohno H. 2023 Validity condition for the local sheath impedance boundary condition and a nonlocal generalization *AIP Conf. Proc.* **2984** 060002
[23] Helou W. *et al* 2015 *Fusion Eng. Des.* **96** 473–6
[24] Hillairet J. *et al* 2015 Ion cyclotron resonance heating systems upgrade toward high power and cw operations in west *AIP Conf. Proc.* **1689** 070005
[25] Colas L., Jacquot J., Hillairet J., Helou W., Tierens W., Heuraux S., Faudot E., Lu L. and Urbanczyk G. 2019 *J. Comput. Phys.* **389** 94–110
[26] Myra J. 2017 *Phys. Plasmas* **24** 072507
[27] Stix T.H. 1992 *Waves in Plasmas* (Springer)

[28] Campos Pinto M. and Després B. 2017 *SIAM J. Math. Anal.* **49** 3637–70
[29] Tierens W. and Colas L. 2021 *J. Plasma Phys.* **87** 905870405
[30] Milanesio D., Meneghini O., Lancellotti V., Maggiora R. and Vecchi G. 2009 *Nucl. Fusion* **49** 115019
[31] Tierens W., Paulus F. and Bilato R. 2023 *Phys. Plasmas* **30** 102102
[32] Gunn J. and Pascal J.Y. 2011 *Rev. Sci. Instrum.* **82** 123505
[33] Behrisch R. and Eckstein W. 2007 *Sputtering by Particle Bombardment: Experiments and Computer Calculations From Threshold to MeV Energies* vol 110 (Springer)
[34] Younkin T. *et al* 2021 *Comput. Phys. Commun.* **264** 070005